Spatial and temporal control of Archean tectonomagmatic regimes

Eric D Vandenburg, Oliver Nebel, R. Hugh Smithies, Fabio A Capitanio, Laura Miller, Peter A Cawood, Marc-Alban Millet, Emilie Bruand, Jean-François Moyen, Xueying Wang, et al.

Spatial and temporal control of Archean tectonomagmatic regimes

Eric D. Vandenburg, Oliver Nebel, R. Hugh Smithies, Fabio A. Capitanio, Laura Miller, Peter A. Cawood, Marc-Alban Millet, Emilie Bruand, Jean-François Moyen, Xueying Wang, Yona Nebel-Jacobsen

PII: S0012-8252(23)00106-X

DOI: https://doi.org/10.1016/j.earscirev.2023.104417

Reference: EARTH 104417

To appear in: *Earth-Science Reviews*

Received date: 6 December 2022

Revised date: 27 March 2023

Accepted date: 9 April 2023

Please cite this article as: E.D. Vandenburg, O. Nebel, R.H. Smithies, et al., Spatial and temporal control of Archean tectonomagmatic regimes, *Earth-Science Reviews* (2023), https://doi.org/10.1016/j.earscirev.2023.104417

Spatial and temporal control of Archean tectonomagmatic regimes

Eric D. Vandenburg[1]*, Oliver Nebel[1], R. Hugh Smithies[2], Fabio A. Capitanio[1], Laura Miller[1], Peter A. Cawood[1], Marc-Alban Millet[3], Emilie Bruand[4], Jean-François Moyen[5], Xueying Wang[1], and Yona Nebel-Jacobsen[1,6]

[1]School of Earth, Atmosphere and Environment, Monash University, Melbourne, VIC 3800, Australia.

[2]Department of Mines, Industry Regulation and Safety, Geological Survey of Western Australia, Perth, WA 6004, Australia.

[3]School of Earth and Environmental Sciences, Cardiff University, Cardiff, UK.

[4] Geo-Ocean department, Université Bretagne Occidentale, CNRS, Plouzané, France.

[5]Université Lyon, UJM, UCBL, ENSL, CNRS, LGL-TPE, Lyon, France.

[6] Faculty of Arts and Education, Deakin University, Burwood, Victoria 3125, Australia.

***Correspondence to:** Eric D. Vandenburg (eric.vandenburg@monash.edu)

Abstract

Secular trends in plutonic whole-rock geochemistry pose critical, although non-unique, constraints to early Earth tectonics. Here, we present a large whole-rock geochemical (879 collated samples) dataset for granitoids from the Pilbara Craton, Western Australia, applying it to test the link between secular trends and proposed tectonic mechanisms. We show that the spatio-temporal distribution of granitoid trace element geochemistry is constrained within discrete lithotectonic blocks supporting the reconstruction of its tectonomagmatic evolution. Time-sliced geochemical contour mapping of key petrogenetic ratios indicates the craton underwent rifting ~3.2 Ga (billion years ago), marking a transition from predominantly sodic magmatism to a broader magmatic compositional spectrum. Our results demonstrate that rift-assisted breakup of proto-cratons is a viable craton growth mechanism. We identify a possible evolutionary sequence beginning with drips and upwellings below a Paleoarchean mafic plateau, which is subsequently dismembered by rifting. These plateau fragments form rigid blocks in the Mesoarchean, between which weaker, thinner crust accommodates minor convergence and divergence manifested as short-lived mobile lid-like features before stabilization. We conclude that these features do not require an active lid, plate tectonic regime.

Keywords: granitoids, Pilbara Craton, continental crust, sluggish lid, dripduction, geochemistry.

Abbreviations: EPT, East Pilbara Terrane; WPS, Western Pilbara Superterrane; CPTZ, Central Pilbara Tectonic Zone; EPTRE, East Pilbara Terrane Rifting Event.

MAIN TEXT

1. Introduction

Cratons are the oldest stable blocks of lithosphere on Earth, providing insight into the geological processes of the planet's early history, dating as far back as 4.02 billion years ago (Ga) (1, 2). However, disentangling the complex deformation and tectonomagmatic evolution of Earth's oldest preserved crustal fragments is fraught with difficulty. Despite its crucial importance to the understanding of our planet, constraining the tectonic and crustal evolution of the early Earth remains contentious (3)

Reconstructions of the crustal evolution in the Archean Eon (4.0-2.5 Ga) are predominantly based on the chemical composition of the plutonic rocks of the tonalite-trondhjemite-granodiorite (TTG) series. These plutons trace the evolution of the continental crust, representing felsic, partially molten derivatives of a mafic protolith that was in parts hydrated and buried to a depth of 25-50 km, compatible with amphibolite to eclogite facies conditions (4-6). Reconstructions using chemistry rely on the inference that the analyzed samples are representative of Archean crust spatially within and among cratons, over hundreds of millions of years. Secular changes in geochemical proxies within these plutons have led to the development of models of crustal maturation throughout the Archean (e.g., 7-9), which are complemented by numerical models of geodynamic crust-mantle evolution (e.g., 3, 10-12). These argue for crustal evolution throughout the Paleoarchean (3.6-3.2 Ga), reflecting the maturation of proto-cratonic crustal blocks in a poorly mobile-lid environment, with granitoid magmatism generated by the melting of basaltic crust. Subsequently, these proto-cratons became stable entities during the Mesoarchean (3.2-2.8 Ga), commonly accompanied by widespread reworking of pre-existing granitoid crust. In the Neoarchean (2.8-2.5 Ga), crustal maturation is linked to further changes in

magmatism, which are invoked by some to reflect a fully mobile lid, plate tectonic regime (e.g., 13). However, changes in the chemical composition of TTGs can be interpreted as reflecting distinct pressure-temperature conditions reflecting variations in crustal depth, source hydration or even a change of the source rock chemistry itself (e.g., 5, 14, 15). Complications arise through the fact that plutonic rocks generally do not represent true liquid compositions but rather cumulate mushes, blends of melts and/or fractionated melts (e.g., 16-19). Hence, any Archean geodynamic reconstructions based on TTG chemistry are highly conjectural and will likely result in non-unique solutions.

Computational modelling has constrained the conditions in which crustal formation and evolution may have occurred. Different scenarios have been proposed, ranging from the effect of a plume (20, 21), to lithospheric rifting (10-12), peeling (22-25), crustal sinking (4), and even large bolide impacts (23,24), providing the environments for juvenile crust formation, its reworking, and evolution towards more differentiated compositions. However, similar thermobaric (temperature/pressure, T/P) and source conditions may be found in different tectonic environments, and these petrogenetic constraints cannot discern tectonic mechanisms (9, 10). Several modelling studies have tested the viability of present-day (plate) tectonics under elevated mantle temperatures considered to be representative of the Archean (e.g., 26-29), showing possible mobility and episodic plate margin-like processes. However, several lines of evidence support the idea of a poorly-mixed Archean mantle (e.g., 30, 31) beneath a sluggish lid (e.g., 3), in which high mobility may have been episodic, allowing for a range of tectonic behaviors (11). However, the starting criteria that inform the possible paths of geodynamic evolution are poorly defined, and the interpretation of observations from Archean cratons remains ambiguous. Thus,

the critical validation of these mechanisms is hampered by the paucity of the geological record and the non-uniqueness of geochemical tracers.

Additionally, there remain outstanding questions about how the mechanisms of craton formation may operate in the global tectonic regime of the early Earth. From 3.3 Ga onwards, there is considerable debate about the timing of changes in tectonic regimes on Earth and the accompanied diversification of tectonomagmatic settings. Based on secular changes in geochemical proxies, some studies argue for the initiation of some sort of plate tectonics between 3.3 and 3.0 Ga (global geochemical datasets of TTGs; e.g., 7), whereas others suggest a transition towards plate tectonic initiation by 3.25 Ga (Hf in black shales, 32), 3.0 Ga (based on the chemistry of terrigenous sedimentary rocks, e.g., 33; zircons, e.g., 34) and even as late as 2.5 Ga (chemistry of basaltic rocks through time; e.g., 8, 35). However, the employed proxies are non-unique (i.e., 33 vs 36), and subtle secular changes do not conclusively relate to a shift in geodynamic modes.

Here, we adopt the process of statistical geochemistry to test the link between secular trends and proposed tectonic mechanisms, focusing on spatio-temporal distributions within the Pilbara Craton. Statistical approaches usually group Archean granitoids to elucidate global changes in geodynamic regimes (e.g., 7, 9, 37). Although valid, this approach may be affected by *a-priori* assumptions on the statistical methods or, when merged in global datasets, may introduce significant noise (e.g., 13). Moreover, within cratons, lithotectonic blocks may evolve as exotic entities, such that the diversity of the geodynamic environs and evolution may be lost when data from different provinces are pooled. In this work, we statistically interrogate a large dataset from a single craton, the Pilbara Craton, with a focus on the spatio-temporal distribution of the rocks.

The Pilbara Craton, Western Australia, is divided into seven distinct lithotectonic blocks that contain some of the oldest successions of mafic-ultramafic and felsic volcanic rocks and subordinate sedimentary rocks on Earth (38). These volcano-sedimentary sequences were deposited in multiple episodes between 3.54 and 2.63 Ga, accompanied by several pulses of granitic magmatism between 3.59 and 2.83 Ga. The craton comprises the East Pilbara Terrane (EPT), the Karratha, Regal, and Sholl terranes, collectively referred to as the West Pilbara Superterrane (WPS), the Central Pilbara Tectonic Zone (CPTZ), and the Kurrana Terrane (Fig. 1). The EPT, Kurrana Terrane and Karratha Terrane shared a common Paleoarchean history (herein referred to as the Ancestral Pilbara Block) and were separated during the main stage of the East Pilbara Terrane Rifting Event between 3.22 and 3.18 Ga (39). This event produced the Regal Terrane and CPTZ; the Sholl Terrane was subsequently constructed within the latter. These blocks are well-preserved and only affected by lower greenschist facies (locally amphibolite facies) metamorphism (40, 41). The proposed stabilization of the craton at ca 2.9 Ga (42), combined with the lack of subsequent reworking and large-scale deformation events, makes the Pilbara a prime candidate for studying the early tectonomagmatic regimes of Archean cratons.

Even on the scale of an individual craton, confounding factors otherwise obscured in simple bivariate analysis may be imparted by paleogeography (i.e., differences in evolution timescales for various lithotectonic components of cratons; 43, 44). Hence, we use granitoid-derived geochemical contour mapping of the Pilbara Craton to highlight spatio-temporal variations in geochemical proxies, which allow the reconstruction of its petrogenetic evolution and test its compatibility with possible geodynamic processes. We then discuss the role of short-lived

divergence in the Pilbara in the geodynamics regime in which the craton formed, which reveals a diversification of tectonomagmatic regimes at the Paleo-Mesoarchean boundary.

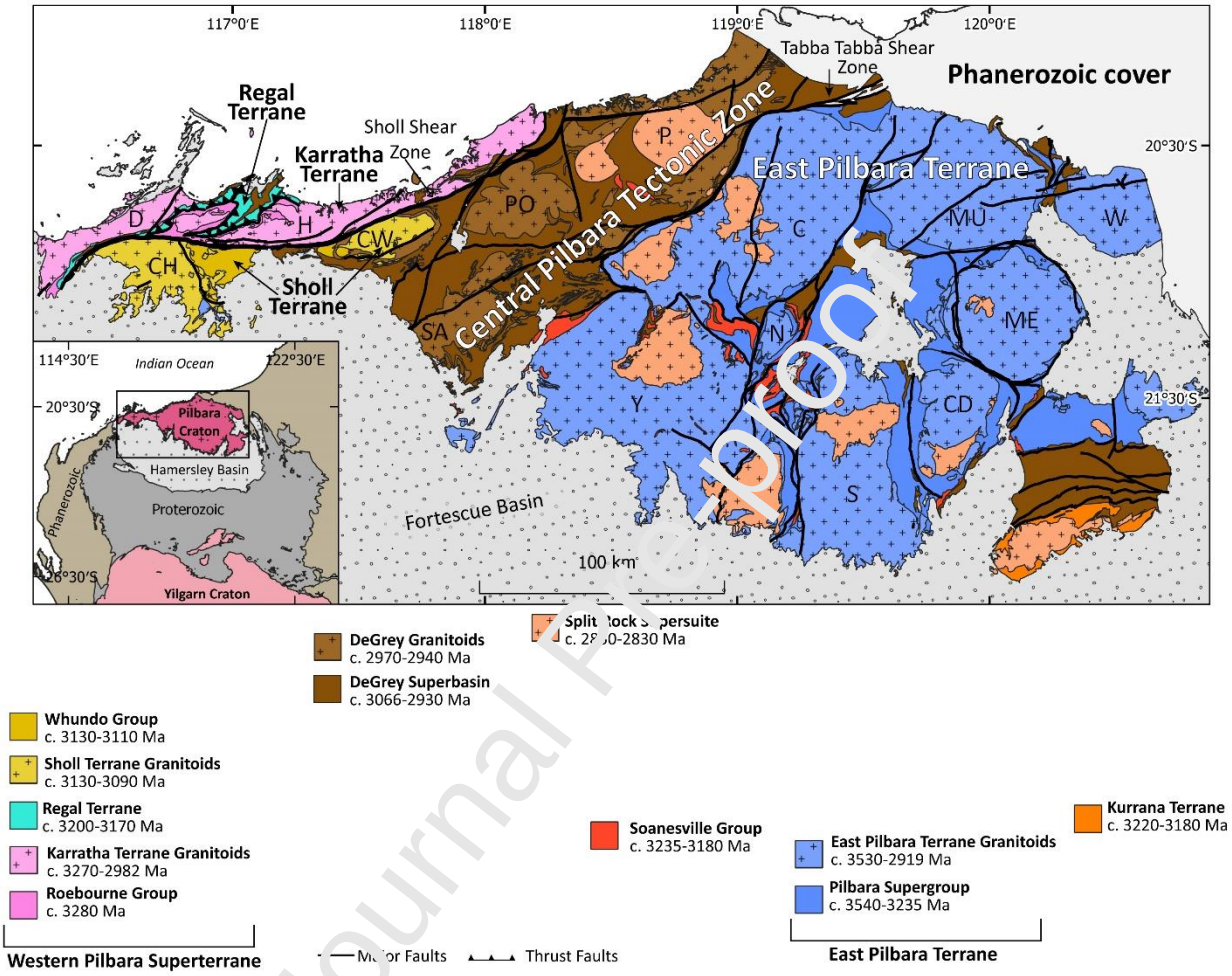

Figure 1. Map of the Pilbara Craton, illustrating the distribution of distinct lithotectonic blocks with different geological histories. Abbreviations correspond to granitoid domes and complexes: C, Carlindi; Y, Yule; N, North Pole; S, Shaw; CD, Corunna Downs; ME, Mount Edgar; MU, Muccan; W, Warrawagine; CH, Cherratta; D, Dampier; H, Harding; CW, Caines Well; PO, Portree; SA, Satirist; P, Pippingarra.

2. Materials and Methods

2.1. Compiled whole-rock geochemistry

In this study, whole-rock geochemical data was compiled from three sources (Data S1):

The first dataset comprises 67 mafic to felsic plutonic samples from the Pilbara Craton, collected by Monash University as part of fieldwork with the GSWA (Geological Survey of Western Australia) in 2019 (YiPi database). These samples range in age from >3.50-2.83 Ga; ages were acquired from other samples from the same locality or from the general age of the pluton from which they were collected. Before analysis, this dataset's samples were cleaned by trimming off weathering rinds with a diamond blade saw. The resulting material was then crushed with a ceramic jaw crusher and disc crusher and milled in an agate ring mill to minimize contamination during preparation. These samples were analysed for major, minor and trace element whole-rock geochemistry at ALS Minerals, Perth, Western Australia. Major and minor element concentrations (Si, Al, Fe, Ti, Mn, Mg, Ca, Na, K, Cr, Sr, Ba, and P) were determined by X-ray fluorescence (XRF) spectrometry on a fused glass disk prepared by fusing a 1:10 sample-flux mix ($LiBO_2$, LiB_4O_7 and $LiNO_3$ flux) (ALS code ME-XRF26), and loss on ignition was determined by thermogravimetric analysis (ALS code ME-GRA05). Lithophile trace elements (including Ba, Ce, Cs, Dy, Er, Eu, Ga, Gd, Hf, Ho, La, Lu, Nb, Nd, Pr, Rb, Sm, Sn, Sr, Ta, Tb, Th, Tm, U, V, Y, Yb, and Zr) were determined by fusing each sample with a flux mix ($LiBO_2$, LiB_4O_7), before dissolving in acid and analysis by ICP-MS (ALS code ME-MS81). Base metal (Cr, Cu, Ge, Mo, Ni, Pb, Sb, Sc, Zn), Be, and Li concentrations were determined by dissolving samples with a four-acid mixture ($HClO_4$, HNO_3, HF, HCl) followed by analysis via ICP-MS (ALS code ME-MS61L). Total uncertainties for major elements are ≤1.5%, and those for minor elements are <2.5% (at concentrations >0.1 wt.%). Repeat analysis of the OREAS 24b and CCRMP SY-4 reference materials gave RSD values of <5%, and mean concentrations are within

10% of published values (45, 46) for most elements. Blindly inserted single analyses of the USGS RGM-1 and CNS GSR-1 are also within 10% of published values (47,48) for most elements (Data S2). RSD values for duplicate sample analyses are generally better than 5% for most elements (Data S2), and total procedural blanks were negligible relative to analyzed sample concentrations.

The second dataset comprises samples from the GSWA geochemistry database (WACHEM; 49). Ages for these samples were calculated based on their proximity to geochronology samples of the same lithology (50) and the age of the geological unit that they are contained within (based on 1:500,000 bedrock geology; 51). After filtering for lithology and geography (see below), this yielded a range of ages between 3.47-2.83 Ga.

The third dataset consists of samples from the Geoscience Australia (GA) inorganic geochemistry database (GEOCHEM; 52). As with the previous dataset, the ages for these samples were calculated based on their proximity to geochronology samples of the same lithology and the age of the geological unit that they are contained within, yielding an age range of 3.50-2.83 Ga.

Prior to filtering for quality control purposes, the GSWA and GA databases were clipped to only contain samples from the exposed portions of the >2.80 Ga Pilbara Craton. The Rocklea, Sylvania, Rat Hill, Milli Milli, Rooney, Springo and Wyloo inliers were excluded from the dataset due to their distance from the main exposed portion of the craton.

Data were filtered for quality using the following criteria:

(i) Of the intermediate-felsic intrusive lithologies considered, we excluded pegmatites, aplites, enclaves, and alkaline intrusives to mitigate against samples with exotic (very compositionally-evolved/fractionated) compositions.

(ii) All samples contain <80 wt. % SiO_2 and <6 wt. % loss-on-ignition (LOI).

(iii) Elements affected by alteration were avoided, such that we focused on HFSE and REE. Where more mobile elements were used, such as the LILE, we used ratios of these elements to mitigate the potential effects of mass loss or gain. Furthermore, samples were not filtered by K or K/Na due to the potential bias that this may impart by affecting the proportion of the 'enriched TTG' component (53, 54).

(iv) Outliers were removed from individual contour maps and diagrams so as to not impart potential bias on the observations.

The filtered database comprises 184 samples from WACHEM and 628 samples from GEOCHEM, which with the 67 fieldwork samples, gives a total of 879 (Data S1). These samples cover the main exposed portions of the Pilbara Craton, ranging in age between 3.50 and 2.83 Ga (Fig. S1, S2, S3, S4).

2.2. Granitoid classification

Archean granitoid plutons are compositionally diverse, a reflection of their complex genesis (54, 55), but are generally divisible into three main groups: the TTG series, potassic granites and sanukitoid series. The TTG series is characterized by $K_2O/Na_2O \leq 0.6$, 3-7 wt. % Na_2O, SiO_2 >64 wt. %, Sr/Y >20, and low MgO and Fe_2O_3 (average Mg# 0.43) (56, 57). We also include low Sr/Y (<20) sodic granites within this grouping; as such, we chose to classify TTGs as sodic granitoids *sensu lato* for the sake of simplicity. Intra-crustal reworking of these TTGs is inferred to have produced potassic granitoids, characterized by $K_2O/Na_2O \geq 0.8$ and SiO_2 >64 wt.%, and

low MgO and Fe_2O_3 (6). These melts are, therefore, tertiary crustal melts and the most mature granitoids found in cratons (44). Sanukitoids are typically defined as having high Mg, Cr, Ni and large-ion lithophile element concentrations at SiO_2 > 55 wt.%, which is consistent with derivation from metasomatically enriched lithospheric mantle (56, 58, 59). Here, we adopt these definitions to characterize the plutons of the Pilbara craton, using a hybrid approach that combines methodologies from Laurent *et al.* (13), Mole *et al.* (60), Moyen and Martin (6), and Smithies *et al.* (61). We place the dividing line between sodic and potassic granitoids at K_2O/Na_2O = 0.7 to note the potential presence of hybrids (transitional TTG, 44, 62) and avoid the effect of increases in Sr/Y due to source enrichments and multiple reworking events as a natural consequence of the way these rocks form (54). Sodic and potassic granitoids can be further divided into low Sr/Y (Sr/Y<40) and high Sr/Y (Sr/Y >40), which broadly reflects the garnet/plagioclase ratio of the residue of the source protolith after melting (61) and increases with pressure (Sr (Y) is (in)compatible in plagioclase, which is only stable at low pressures, whereas Y (Sr) is (in)compatible in garnet, which stabilizes at higher pressures) (Fig. S2A); low Sr/Y corresponds to the low-pressure (LP) group (63). Sr/Y can also increase with fluid-fluxed melting (e.g., 15). The high Sr/Y groups were further divided into medium- (MP) and high-pressure (HP) groups based on their Nb contents, potentially reflecting the stability of rutile in the source protolith (Nb is compatible in rutile, which stabilizes in the melting residue at high pressures; e.g., 7, 60). We classify sanukitoids based on a range of element relations captured in the K_2O/Na_2O-FMSB-A/CNK ternary diagram of (13), which tracks the relative contributions of meta-igneous mafic, fluid-metasomatized lithospheric mantle and Al-rich felsic crustal components, respectively (Fig. S2B). In this classification, sanukitoids are characterized by high

FMSB ($[FeO_T + MgO]_{wt.\%}$ * $[Sr + Ba]_{wt.\%}$) signature indicative of interactions between mantle peridotite and incompatible element-enriched components.

2.3. Interpolation methods

Trace-element contour maps were constructed in ArcGIS using the inverse distance-weighted interpolation (IDW) function of the Spatial Analyst toolbox; input parameters included a power of 2, a variable search radius, and a maximum number of points of 15. This method operates under the assumption that features that are located proximally are more similar than those located distally to one another. IDW predicts values for unmeasured locations by using the measured values surrounding the prediction location, with the influence decreasing as a function of distance away from the interpolated point. While the exactness of this method can lead to misleading "bulls-eye" features, this same effect has been a valuable asset in previous geochemical mapping studies (e.g., 60, 64, 65), as the maximum and minimum points on the interpolation surface can only occur at actual data points.

The geometric interval classification scheme was used to create class intervals for the contour maps. It creates these breaks based on class intervals that have a geometric series, with the algorithm creating geometric intervals by minimizing the sum of the square of the number of elements in each class. This ensures that the range of each class has roughly the same number of values in each class while maintaining consistent change between intervals. These classes were derived from the full, non-time sliced dataset to ensure consistency between time slices.

3. Results

We present major and trace element whole-rock analyses of 67 new granitoid samples along with previously published data (*n*=814) (49, 52) for the main exposed portions of the Pilbara Craton.

Within our dataset, granites predominate, with subordinate trondhjemite, tonalite, granodiorite, diorite, and quartz monzonite (Fig. S3). This data forms the basis for geochemical contour maps of the craton, split at time intervals corresponding to the Paleo- and Mesoarchean.

3.1. Trace element contour mapping and the necessity for time slicing

In addition to the classification of the plutons based on geochemistry, we have investigated all samples in a spatio-temporal context. Our time-sliced, inverse distance-weighted (IDW) interpolation-derived, trace element contour maps reveal geographic and temporal trends that would otherwise be obscured on bivariate element-element, ratio-ratio or element/ratio-time diagrams (Fig. 2, Fig. S5). In particular, spatio-temporal variations in the trace element ratios, Sr/Y, Sm/Yb_{PM} (Sm/Yb ratios normalised to primitive mantle values of [66]), La/Sm, Zr/Ti and Ba/Th were found to reveal insights into the evolution of the Pilbara craton.

The validity of the IDW interpolation-derived contour maps was investigated using the ratios Sr/Y and Sm/Yb_{PM}. Viewing the entire dataset, areas of high values on Sr/Y and Sm/Yb_{PM} on IDW interpolation-derived contour maps broadly coincide with the medium- and high-pressure lithologies (Fig. 2). Likewise, areas characterised by zones of low Sr/Y and Sm/Yb_{PM} coincide with low-pressure granitoid groups. The low and high Sr/Y and Sm/Yb_{PM} areas identified by the IDW contour maps correspond to groups of low and high points on Sr/Y and Sm/Yb_{PM} scatter diagrams, respectively. These observations demonstrate the effectiveness of IDW interpolation contour maps in resolving geographical relationships with geochemical datasets.

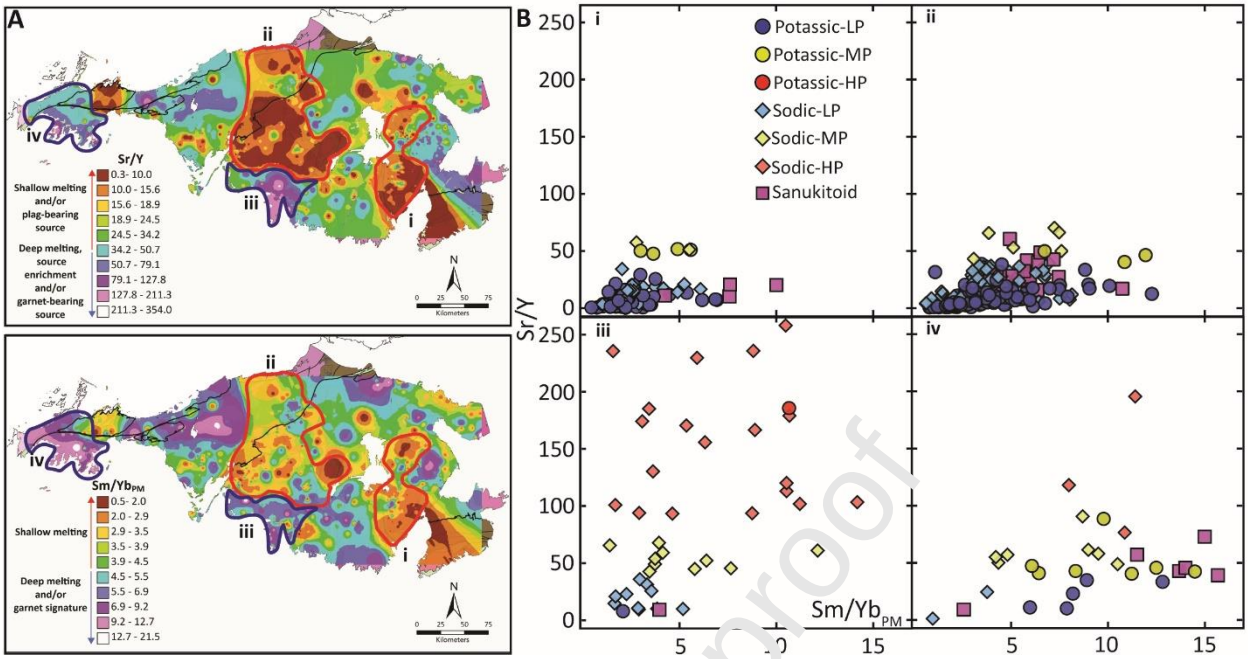

Figure 2. Covariation between zones of highs and lows in trace element contour maps and their corresponding data subsets in diagrams of Sr/Y versus Sm/Yb_{PM}. (**A**) contour maps of Sr/Y and Sm/Yb_{PM} for the entire dataset of Pilbara granitoids. Highs are circled in blue, and lows are circled in red; numerals denote the corresponding panels in (B). (**B**) plots of Sr/Y versus Sm/Yb_{PM} showing the data subsets highlighted in the contour maps in (A) (denoted by numerals). Areas of high values (blue and purple hues) correspond to data subsets with a predominance of high- (red symbols) and medium-pressure (yellow symbols) lithologies, whereas areas of low values (red and orange hues) correspond to data subsets dominated by low-pressure (blue symbols) lithologies. Shapes correspond to magmatic series (sodic magmas are diamonds, potassic magmas are circles, and sanukitoids are squares). The samples analyzed here can be found in Data S1, and the sample locations are plotted in Fig. S1. Abbreviations: LP, low-pressure; MP, medium-pressure; HP, high-pressure.

Plotting all of the data rather than as subsets as a function of time has the potential to obscure the temporal evolution of the craton. As such, the dataset was broken into time intervals corresponding to the Paleo- and Mesoarchean (Figs. 3, 4). We chose 3.2 Ga as the dividing line for the time slices because of the lull in data between 3.23 and 3.12 Ga (n=36), which is the smallest sample size for a single ~0.1 Gyr interval by a significant amount, thus providing a wide natural break in the data (Fig. S4). For the Paleoarchean slice, we have only a single lithotectonic block, the Ancestral Pilbara Block (contour extents in Fig. 3), essentially composed of the composite Karratha and East Pilbara terranes, albeit joined at this time. The younger slice contains three lithotectonic blocks: WPS and EPT, now separated by the CPTZ.

3.2. Time-sliced trace element contour maps

Both Sr/Y and Sm/Yb_{PM} are interpreted to be positively correlated with the increasing pressure of melting of TTG sources, shifting from plagioclase-stable conditions at low values (Sr is compatible in plagioclase) to garnet ± rutile-stable conditions at high values (Y and HREE are compatible in garnet) (5, 6, 54, 67). For the time period prior to 3.2 Ga (i.e., Paleoarchean), maps of Sr/Y and Sm/Yb_{PM} show similar geographical distributions (Fig. 3A, B). In the EPT, low Sr/Y and Sm/Yb_{PM} contours are concentrated in the entirety of Corunna Downs and North Pole (+ northeasternmost Yule) domes and the portions of the Mount Edgar and Muccan domes closest to the Marble Bar sub-basin (Figs. 1, 3A, B). In contrast, areas of high Sr/Y and Sm/Yb_{PM} are concentrated mainly in the western Shaw, southern Yule and eastern Mount Edgar domes, with smaller zones interspersed throughout each dome except for Corunna Downs Dome. The other portion of the Ancestral Pilbara Block, the Karratha Granitoid complex of the Karratha Terrane, largely displays moderate-pressure signatures. After 3.2 Ga, the Ancestral Pilbara Block

splits into the East Pilbara and Karratha terranes, respectively. High Sr/Y and Sm/Yb_{PM} signatures largely disappear from the EPT, shifting mainly towards the Sholl Terrane and CPTZ (Fig. 4A, B). The EPT broadly forms a zone of low Sr/Y and $Sm/Yb_{PM,}$ except for the southern Yule and Shaw domes, which form smaller zones of high values. In contrast, to the west of the EPT, the only two large zones of low Sr/Y and Sm/Yb_{PM} are in the Karratha and Regal terranes of the WPS and within the Satirist Monzogranite and Myanna Leucogranite units of the Sisters Supersuite within the newly established CPTZ.

Contour maps of La/Sm show similar patterns to those observed for Sr/Y and Sm/Yb_{PM} (Figs. 3C, 4C). Because La/Sm is positively correlated with the degree of fractional crystallization and negatively correlated with the degree of partial melting of a source, increases in the pressure of melting might be interpreted to correspond to decreases in the degree of melting of the source

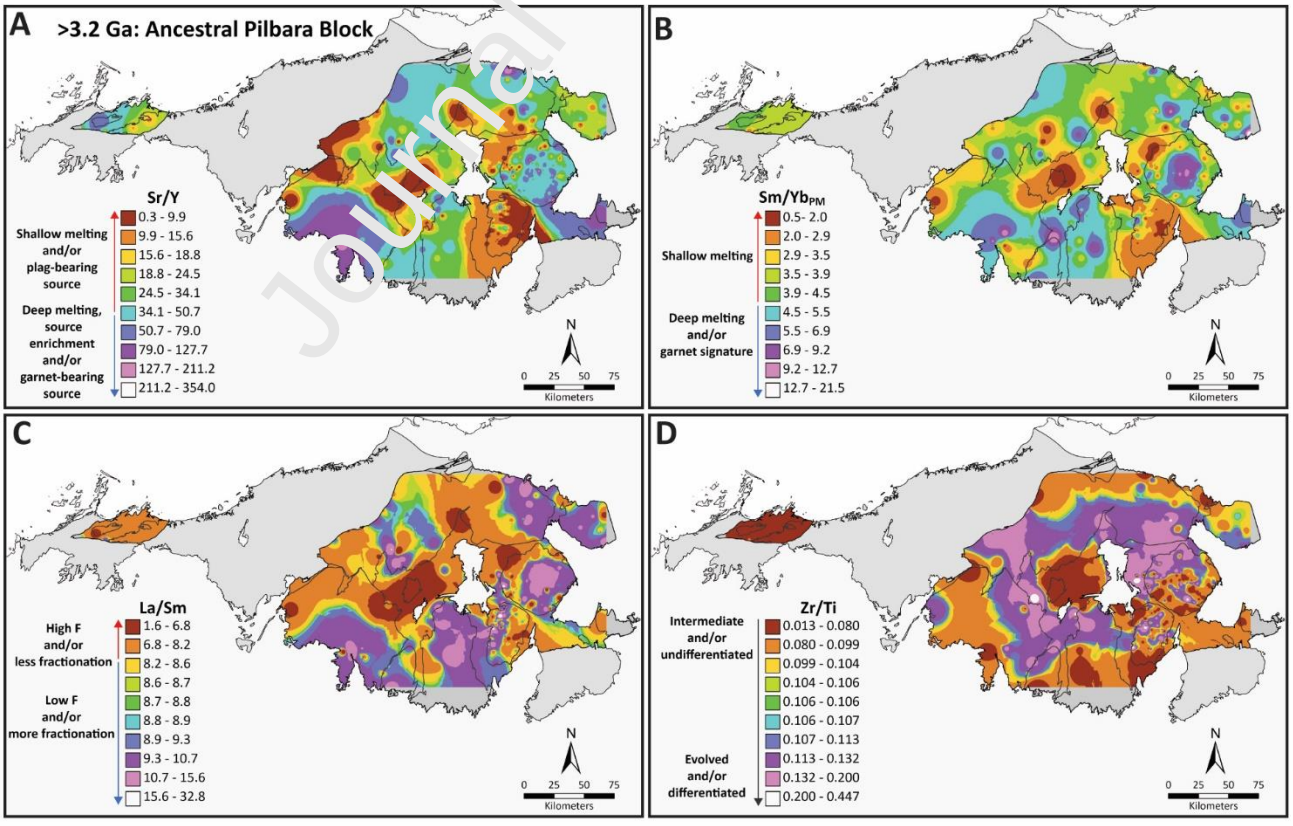

Figure 3. Trace element contour maps for a >3.2 Ga time slice within the exposed portions of the Pilbara Craton. Contour maps of (**A**) Sr/Y and (**B**) Sm/Yb_{PM} suggest the EPT (easternmost block) is initially the locus of relatively deep and high-pressure melting, where lower-degree melting occurs in the garnet stability field that we interpret as lower-crustal drips (blue and purple hues), interspersed by areas of thinner crust and crustal hot zones where higher-degree melting at shallow, plagioclase-stable depths occur (red and orange hues). (**C**) The contour map of La/Sm suggests magmas that formed at the base of thick crust or within deep lithospheric drips were typically produced by lower degrees of melting (blue and purple hues) or are more fractionated than magmas formed at shallower depths within the crust (red and orange hues). (**D**) Zr/Ti contours indicate that relatively juvenile granitoid magmatism is largely confined to the margins of the EPT (red and orange hues), flanking a core of evolved magmatism (blue and purple hues). Grey areas within the craton represent areas of crust younger than 3.2 Ga. Solid black lines within contoured areas correspond to the simplified boundaries of granitoid complexes.

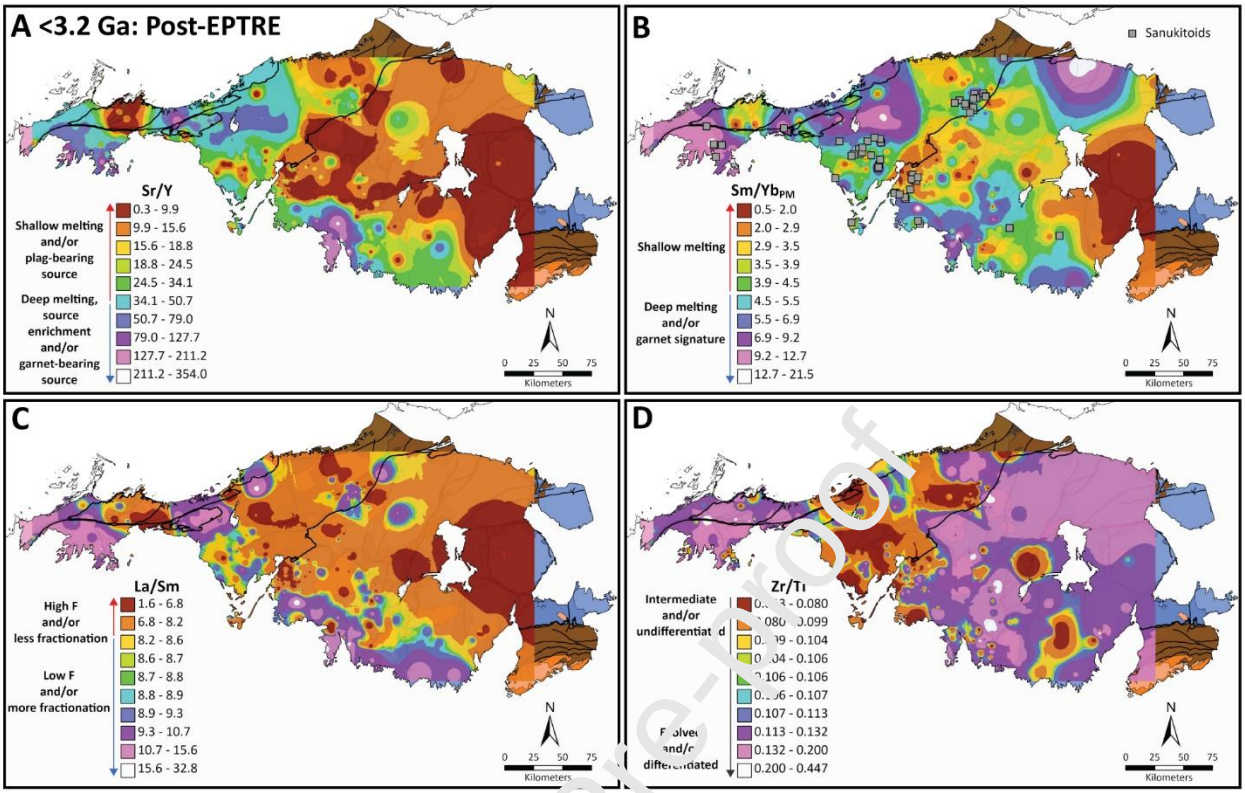

Figure 4. Trace element contour maps for a <3.2 Ga time slice within the exposed portions of the Pilbara Craton. Contour maps of (**A**) Sr/Y and (**B**) Sm/Yb$_{PM}$ suggest that subsequent to the East Pilbara Terrane Rifting Event (EPTRE)-triggered breakup of the Ancestral Pilbara Block at 3.2 Ga, high pressure, lower degree melting in the garnet stability zone shifts towards the margins of the exposed craton, occurring predominantly within the Sholl Terrane and the southern margin of the EPT, potentially above asymmetric downwelling zones. Localized zones of high Sr/Y and Sm/Yb$_{PM}$ within the CPTZ are associated with sanukitoid intrusions (grey squares, (B)). (**C**) La/Sm contours demonstrate that **"**dripduction" zone magmas that formed within deep asymmetric downwellings were typically produced by lower degrees of melting (blue and purple hues) or are more fractionated than magmas formed at shallower depths within the crust (red and orange hues). (**D**) Zr/Ti contours are consistent with the restriction of juvenile magmatism to the CPTZ (red and orange hues), whereas evolved magmatism comprises the vast

majority of the EPT and WPS (blue and purple hues). The thick black lines within the maps represent lithotectonic block boundaries (see Fig. 1 for more information).

and/or increases in the degree of fractional crystallization during ascent.

Maps of Zr/Ti track the degree of evolution of granitoids across the craton (Figs. 3D, 4D). Zr/Ti is negatively correlated with Mg# (Fig. S6) and can therefore be used as an index of magmatic differentiation and has been previously used to classify the degree of differentiation of different magmatic series (e.g., 68, 69). The pre-3.2 Ga Ancestral Pilbara Block is characterized by a central core of high Zr/Ti (with the exception of North Pole Dome) and is surrounded by areas of low Zr/Ti that include the Karratha Terrane (Fig. 3D). After the East Pilbara Terrane Rifting Event at 3.2 Ga, the vast majority of the EPT and WPS shift to high Zr/Ti and the newly-formed CPTZ becomes the main zone of low Zr/Ti (Fig. 4D).

The geographical variations in Ba/Th are also very similar to those of Sr/Y (Fig. S7). Ba/Th increases with an increasing fluid contribution towards the source of melting (e.g., 70), but it can also increase with increasing pressure (71). In both pre-and post-3.2 Ga time slices, areas of high Sr/Y largely correspond to zones of moderate to high Ba/Th. However, in the post-3.2 Ga time slice, the spatial distribution of ultra-high Ba/Th values increases (Fig. S7B, white contour). Alternatively, this shift may be due to increasing contributions of an enriched source component.

4. Discussion

4.1. Inferences on petrogenesis from contour mapping

The trace element contour mapping provides constraints to the petrogenetic environments that characterize the evolution of the individual blocks. Due to the role that pressure plays in controlling the Sr/Y and Sm/Yb_{PM} ratios of a magma, zones of high Sr/Y and Sm/Yb_{PM} may correspond to areas of thick crust, where melting in the garnet stability field can be achieved, whereas zones of low Sr/Y and Sm/Yb_{PM} (e.g., Corunna Downs dome) correspond to areas of thin crust and/or crustal hot zones (62). Prior to its separation from the EPT, the Karratha Terrane was also characterized by moderate-depth melting and likely corresponded to a zone of medium crustal thickness (Fig. 3A, B). The different distributions of Sr/Y and Sm/Yb_{PM} in the Mesoarchean suggest changes in the petrogenetic processes of the craton accompanied by the construction of the CPTZ and Sholl Terrane. The lows in Sr/Y and Sm/Yb_{PM} within the composite Karratha-Regal terranes and the majority of the EPT suggest that post-3.2 Ga magmatism emplaced into Paleoarchean crust had relatively shallow origins; this is consistent with relatively shallow melting during crustal reworking to produce the Split Rock Supersuite at 2.85 Ga (72). The high Sr/Y and Sm/Yb_{PM} zone within the southern portion of Yule Dome and the appearance of elevated ratios within the Shaw Dome may represent a shift towards deeper melting in the garnet stability field (see below). This event is inferred to have been coeval with the intrusion of the Elizabeth Hill Supersuite. The high Sr/Y and Sm/Yb_{PM} values across the Sholl Terrane suggest that it was constructed by high-pressure garnet-stable regime magmatism coinciding with the Railway, Orpheus, and Maitland River supersuites. Except for the southern Portree Suite intrusion, areas of high Sr/Y and Sm/Yb_{PM} in the CPTZ are associated with sanukitoids emplaced as part of the Indee Suite. (Fig. 3A, B). While there are sparse occurrences of sanukitoids across the craton, their high concentration proximal to the Tabba Tabba Shear Zone suggests that structural heterogeneities played an important role in their petrogenesis,

reflecting areas conducive to the extraction of higher-pressure lithospheric mantle-derived melts (13, 56).

It is noteworthy that recent petrologic studies (e.g., 17-19) have suggested that high and low Sr/Y values in "high-pressure" and "low-pressure" TTGs can be produced by cumulate fractionation processes rather than source depth. As with any plutonic rock, true liquid compositions can be obscured by such processes. However, we rule this out on a larger scale due to the replication of Sr/Y contours by Sm/Yb_{PM}, the occurrence of high-pressure sodic lithologies at reasonably low Zr/Ti, and the oblique mantle-TTG mixing trends for high and low-pressure TTGs on a Th/Yb-Nb/Yb plot (Fig. S8); fractionation would be expected to produce trends parallel to the mantle array. In fact, high-pressure TTGs form an array that is more perpendicular to the mantle array than low-pressure TTGs.

Several studies have also illustrated the potential confounding effects of source enrichment that can complicate any simple interpretation of Sr/Y as a depth of melting proxy (e.g., 54, 67, 73, 74). In some cases, magmas generated from enriched sources at low to moderate pressures can have Sr/Y ratios similar to those generated from non-enriched sources at high pressure (63). Given the identification of ca. 3.5 Ga LREE- and LILE-enriched basalts and basaltic andesites from the Coucal Formation of the Pilbara Supergroup (75), the metabasalt protoliths of TTG partial melts were likely characterized by variable degrees of enrichment. Thus, in the absence of other data, Sr/Y contour maps cannot reliably trace the depth of melting. However, two lines of evidence suggest that the enriched component is a relatively minor contributor to medium- and high-pressure signatures. First, Sr/Y shows a broad, negative covariation with the melting- and fractional crystallization-independent enrichment parameter ΔRb ($Rb_{(ppm)} - [5SiO_{2\,(wt.\%)} - 220]$) of Moyen *et al.* (63) (Fig. S9A). The predominance of high Sr/Y values at highly negative ΔRb

suggests that most high-pressure magmas were sourced from non-enriched protoliths, as enriched protoliths will produce magmas with slightly negative to very positive ΔRb (63). Likewise, the vast majority of samples classified as high-pressure plot in the low-K mafic rock source field of the experimentally-derived AFM-3CaO-5K_2O/Na_2O ternary of Laurent *et al.* (13), as opposed to the high-K mafic rock source field (Fig. S9B). Second, the enriched lithologies of the Coucal Formation have lower Sr/Y than the non-enriched basalts of the Pilbara Supergroup (e.g., Apex Basalt) (75). Therefore, at least in the EPT, any enriched lithologies that may play a volumetrically significant role in sodic melt production would actually result in an underestimation of pressure based on this parameter.

Recent studies have increasingly implicated fluid-fluxed melting in the formation of TTGs, both in the Archean (e.g., 15, 76) and in the Proterozoic (e.g., 77). Unlike fluid-absent melting, which consumes amphibole with plagioclase as a residual phase (e.g., 6, 67, 78), fluid-fluxed melting in metabasalts consumes plagioclase while retaining amphibole in the residuum (77). Because of the compatibility of Sr in plagioclase and HREE in amphibole, fluid-fluxed partial melting processes have the potential to further confound the interpretation of Sr/Y as a depth of melting proxy, as consumption of plagioclase can generate TTGs with high-pressure signatures at moderate depth. Of course, this will only impact Sr/Y significantly until the point at which plagioclase is exhausted from the source protolith and will not occur at P-T conditions outside of the plagioclase stability field. While we agree with proponents that fluid-fluxed melting has been previously overlooked and is a contributor to TTG generation, especially given the high-water storage capacity of komatiites (15,76), several lines of evidence suggest that fluid-fluxed melting is not a significant contributor to the high Sr/Y values observed in the HP lithologies from our dataset. First, while Y is compatible in both amphibole and garnet, the partition coefficients of Y

are such that D_Y^{garnet} is nearly 15 times higher than $D_Y^{amphibole}$ (15.4 vs 1.04; ref. 79). Thus, even if the protolith in question undergoing melting has eight times as much amphibole as garnet by weight, the contribution of garnet towards the bulk partition coefficient of Y will be ~1.8 times that of amphibole. Second, if the high Sr/Y signatures of HP TTG are produced by plagioclase consumption, then they should have (on average) Sr and REE concentrations greater than and equal to that of MP TTGs, respectively. However, the mean of the Sr concentrations and average REE abundances (λ_0; 80) of the HP sodic group is equal to and less than those of the MP sodic group, respectively (Fig. S10a). Fractional crystallization of plagioclase can be largely ruled out as the reason for this trend, as the HP sodic group, on average, exhibits positive Eu/Eu* anomalies (thereby indicating plagioclase accumulation). In contrast, the MP sodic group does not exhibit this anomaly (Fig. S10b). Therefore, in the Pilbara Craton, Sr/Y is a relatively reliable proxy of the depth of melting.

There are several reasons why the general correlation between zones of high La/Sm with Sr/Y and Sm/Yb_{PM} highs exists. One possibility is that magmas that formed at higher pressures were typically produced by lower degrees of melting or have undergone greater fractional crystallization than magmas formed at lower pressures within the crust. There are two possible explanations for how this may occur. First, melting of metabasalt protoliths along lower geotherms at high-pressure garnet amphibolite and eclogite facies generally results in lower melt productivity than melting along higher geotherms at relatively lower-pressure amphibolite and granulite facies (71, 81). Further, geochemical modelling (71) shows that La/Sm at a given melt fraction decreases as the geotherm increases (Data S3). Another possibility is that high-pressure melts experienced more time to undergo fractional crystallization and interact with the

surrounding crust than their low-pressure counterparts during their ascent, where the exclusion of incompatible elements such as La during fractionation produces high La/Sm ratios.

Alternatively, the variations in La/Sm are mainly controlled by the degree of melting of a source, with additional contribution from the degree of enrichment of said source. In this scenario, the pressure of melting plays an insignificant role in controlling La/Sm contents of magmas. Some low-pressure potassic samples have high La/Sm contents similar to those of many high-pressure sodic samples, and a few high-pressure sodic samples have low La/Sm similar to those of low-pressure sodic samples. Albeit, the means of both the sodic and potassic subsets increase as pressure increases (7.57, 9.63 and 11.41 for low-, medium- and high-pressure sodic and 8.19, 10.94 and 11.13 for low-, medium- and high-pressure potassic, respectively; Data S1). This further supports the inferred role of pressure in controlling the La/Sm ratios of magmas while also providing evidence for the subordinate but still significant role of source enrichment.

Areas of low Zr/Ti correspond to the melting of and/or significant interaction with a juvenile component (lithospheric mantle or basaltic crust). In contrast, areas of high Zr/Ti correspond to melting of and/or significant interaction with a reworked component (e.g., granitoids), potentially augmented with the effect of crustal thickness on magmatic differentiation. In the Paleoarchean, the spatial distribution of Zr/Ti contours is consistent with a core of differentiated magmatism surrounded by relatively undifferentiated rims (Fig. 3D). While recent research (e.g., 82, 24) has argued for a hypothetical impact origin for the Pilbara Craton, the superficial resemblance of our Paleoarchean Zr/Ti contour map to the concentric pattern of an impact crater should not be used as evidence to confirm or deny this hypothesis. It should be stressed that this time slice corresponds to ~300 Myr of Earth's history, far longer of a timescale than that on which impact-related magmatism would be expected to occur (e.g., 83).

By the Mesoarchean, the vast majority of the EPT and much of the WPS shift to high Zr/Ti and the newly-formed CPTZ becomes the main zone of low Zr/Ti, and therefore, the locus of relatively juvenile/undifferentiated magmatism (Fig. 4D). This provides further support that by the Mesoarchean, the proportion of granitoids serving as protoliths for intracrustal melting increased, particularly within the EPT, thus likely reflecting differing stages in evolution between lithotectonic blocks.

As already stated, Ba/Th increases with both increasing fluid contributions and pressure, the latter of which may explain its general correlation with Sr/Y. However, the magnitude of each factor's contribution has likely varied. Data from geochemical modelling of TTG generation (71) suggests that for a given pressure, melting of enriched Archean tholeiite (84) under water-saturated conditions produces magmas with Ba/Th greater than those produced by melting under water-undersaturated conditions (Fig. S11A, Data S3). Even correcting for the effects of water content on solidus depression, the Ba/Th content of magmas produced from a water-saturated protolith is slightly greater than that of a water-undersaturated protolith-derived magma for a given melt volume (Fig. S11B). This is not to say that pressure did not impart some control on spatial variations in Ba/Th; the lower median and interquartile range values of Ba/Th for Paleoarchean time intervals potentially suggest that pressure played a greater role prior to the East Pilbara Terrane Rifting Event (Fig. S12). However, water saturation likely had the most significant role after the East Pilbara Terrane Rifting Event.

Crucially, with the exception of Zr/Ti, the geographical patterns observed in the time-sliced trace element contour maps are largely independent of the magmatic series for each petrogenetic ratio (Fig. S13). For example, potassic and sodic subsets display similar geographical patterns within Sr/Y contour maps of Paleoarchean time slices, albeit with a more subdued contrast of patterns

for the potassic subset (Fig. S13A, B). Likewise, similar patterns can be observed within Sm/Yb_{PM} contour maps of Paleoarchean time slices for sodic and potassic subsets (Fig. S13C, D). This is not the case for Zr/Ti contours, which, to some extent, correspond to each magmatic series (Fig S5), meaning that any chemical classification of rock type must be reflected in the contour maps (Fig. S13E, F). Therefore, the time-sliced Zr/Ti contour maps (Figs. 3D, 4D) broadly approximate the locally dominant magmatic series within a given area.

Our depth proxy indicators are also generally insensitive to the differences in the petrogenetic environments between the sodic and potassic series. First, the contribution of the HP sodic sample subset (n = 48) to high Sr/Y values in the contour maps predominates over that of the HP potassic subset (n=7; a statistically insignificant population). As shown in Fig. S9, source enrichment does not significantly control Sr/Y; sodic and potassic samples with high Sr/Y have broadly similar ΔRb values. Furthermore, the relationship between a fractional crystallization-, enrichment-, and melting-independent depth parameter, in this instance ΔSr ($Sr_{(ppm)}$ – [-$20SiO_{2(wt.\%)}$ + 1700]; Ref. 63), and ΔRb (Fig. S14) illustrates that the median values for the high-, medium-, and low-pressure subsets follow the same general trend irrespective of whether they are sodic or potassic (excluding extreme hybrids between sanukitoid and potassic or sodic magmas). Source enrichment decreases with increased depth of melting, albeit with some offset between sodic and potassic groups; however, this is less significant in higher-pressure lithologies. Therefore, samples of different magmatic series can be plotted on the same contour maps without imparting significant compositionally confounding effects.

4.2. Implications for the tectonomagmatic evolution of the Pilbara Craton

Geochemistry alone cannot be employed to deduce geodynamic regimes. However, the addition of space and time constraints may now facilitate further examination of the tectonomagmatic evolution of the Pilbara craton.

The asymmetric distribution of trace element ratio contours within the Ancestral Pilbara Block is most consistent with a Paleoarchean mafic plateau of variable thickness (see 85), potentially located above a thinned lithospheric mantle and one or more mantle upwellings (e.g., 4, 86) (Fig. 5A). The crustal overthickening produced by associated magmatism is followed by lithospheric drips at the base of thickest crust (high Sr/Y, Sm/Yb_N, La/Sm), melting at the base of moderate-thickness crust (moderate Sr/Y, Sm/Yb_N, La/Sm), thin crust and crustal hot zones (low Sr/Y, Sm/Yb_N, La/Sm), producing high-, medium- and low-pressure TTGs, respectively (Fig. 3) (9, 73). Areas of thin crust and crustal hot zones are also more prone to re-melting of TTG plutons to produce minor volumes of potassic magmas (highest Zr/Ti), particularly towards the core of the lithotectonic block where the reworked components are more prevalent.

The tectonic environment in which the Paleoarchean Ancestral Pilbara Block formed implies lithospheric thinning and melting of an overthickened crust which may be reconciled with existing evolutionary models. The occurrence of high-pressure TTG implies the foundering of hydrated crust to mantle depths. However, we rule out a primitive subduction-like setting owing to the lack of large linear features and alignment of rounded contours with the general dome-and-keel geometry of the Paleoarchean EPT, which is more consistent with a plateau-like protocrustal setting (26, 44, 87) and does not show evidence of convergence. Alternatively, the Ancestral Pilbara Block may have formed via local lithospheric thinning and rifting of a protocrust, bordered by thickening and downwelling of the neighbouring lithosphere, dragging the base of the crust to mantle depth. Lithospheric stretching, with thinning and hot mantle upwelling, may

be accommodated along the rift rims by thickening until the lithosphere is gravitationally unstable and founders with its hydrated crust (10). Elsewhere under the thinned lithosphere, thick, buoyant roots form by dehydration of mantle peridotite (12). In this environment, the low-to-high pressure conditions for TTG can be reproduced (88).

The tectonomagmatic evolution of the Pilbara Craton continues at the Paleoarchean-Mesoarchean boundary with the main stage of the East Pilbara Terrane Rifting Event (39) (Fig. 5B). High-pressure TTGs largely disappear from the majority of the EPT by 3.2 Ga. Extension begins to thin and segment the lithosphere, leading to the development of a rift zone where small-scale reworking of pre-existing granitoids into potassic magmas occurs and eventually separates the Karratha Terrane from the EPT, producing the juvenile crust and weaker lithosphere of the Central Pilbara Tectonic Zone (CPTZ) between the two lithotectonic blocks (Fig. 4D). The disappearance of high-pressure TTGs may be reconciled with the inhibition of lithospheric downwellings by a stiffer sub-EPT lithospheric mantle, due to high degrees of mantle melt extraction. The further segmentation of the lithosphere is compatible with the progressive viscosity increase of the depleted mantle lithosphere, forcing strain migration towards the less depleted western portion of the lithotectonic block (10-12).

Following cessation of the main phase of the East Pilbara Terrane Rifting Event at 3.18 Ga, wider tectonomagmatic diversification is achieved (Fig. 5C), manifested by the construction of the Whundo “Arc” basement of the Sholl Terrane on juvenile crust in the CPTZ. The proposed mechanism for the ‘arc” signature and the prerequisite refertilization of the inferred lithospheric mantle sources of sanukitoids is a “dripduction” event (9, 13, 89). This mechanism is characterized by dipping crust dragged along with/by the lithosphere, providing the necessary

conditions of melting to form high- and medium-pressure TTGs (high and moderate Sr/Y, Sm/Yb_N, La/Sm, respectively, variable Ba/Th; Fig. 4), while fluids released from the crustal drip

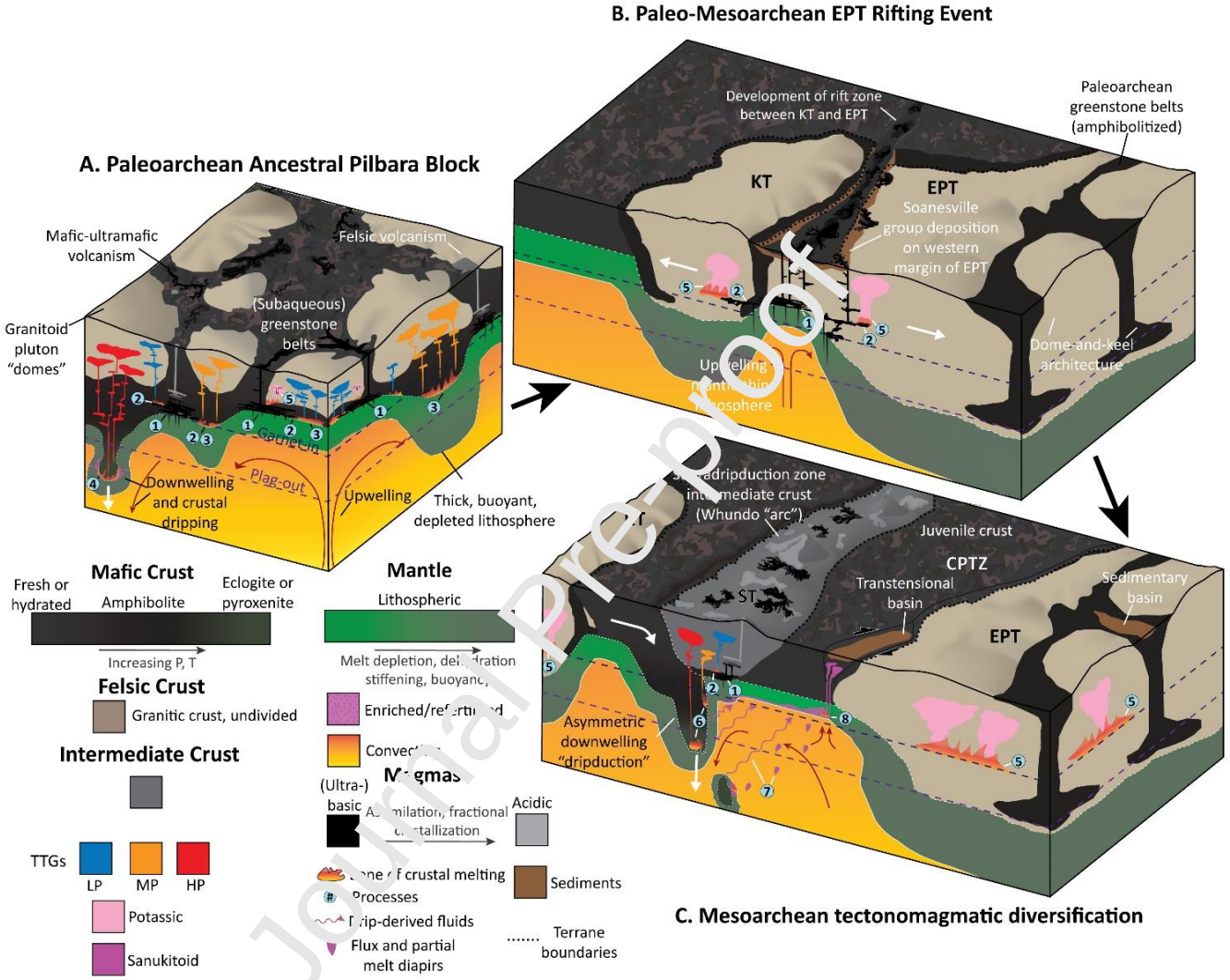

Figure 5. Geodynamic cartoons illustrating the tectonomagmatic diversification of the Pilbara Craton. (A) In the Paleoarchean, the Ancestral Pilbara Block comprises a mafic-ultramafic plateau, where decompression melting in an upwelling mantle triggers the eruption of extensive mafic-ultramafic magmas, which are progressively buried to depth and metamorphosed. Underplating (process 1) and injection (process 2) of these magmas can induce anatexis of amphibolitized mafic crust, forming low-pressure TTG melts. Higher geothermal gradients in

zones of thin and moderate-thickness crust trigger basal melting of metabasaltic crust (process 3), forming low- (LP) and medium-pressure (MP) TTG magmas, respectively. Melting of eclogitized metabasaltic crustal drips (process 4) in downwelling zones forms high-pressure (HP) TTGs. High geothermal gradients and injection of mafic magmas also trigger reworking (process 5) of pre-existing TTG crust, inducing minor potassic magmatism. (**B**) At 3.22 Ga, the extension associated with the long-lived upwelling beneath the Ancestral Pilbara Block begins to thin and segment the lithosphere. This leads to the development of a rift zone, where underplating and injection of mafic-ultramafic magmas trigger small-scale reworking of pre-existing granitoids into potassic magmas and eventually separates the Karratha Terrane from the EPT via the construction of the CPTZ. (**C**) In the Mesoarchean, an asymmetric downwelling in a dripduction zone setting (process 6) within the CPTZ leads to the production of the Whundo "arc" of the Sholl Terrane via fluid-fluxed mantle melting (68). Melting of the slab below the metabasic plagioclase-out isograd (purple dashed line) produces HP TTGs, whereas melting above this isograd produces MP TTGs. Injection and underplating produce LP TTGs. This event metasomatizes the overlying lithospheric mantle (process 7) beneath the CPTZ, where later transtension in pull-apart basins melts the metasomatized mantle (process 8) to produce sanukitoid magmas. Reworking of granitic crust in the EPT and Karratha Terrane produces potassic magmas. Further details are provided in the figure panels and main text.

metasomatize the lithospheric mantle. "Dripduction" zones are the most efficient method of bringing sufficiently hydrated crust to depths where they can induce fluid-fluxed melting within the mantle (9, 27, 90), which is a requisite for producing the geochemical signatures observed in

the calc-alkaline lavas of the 3.12 Ga Whundo Group (91). Here, these are reconciled with the rifting of the neighbouring domain, where the lateral lithospheric stretching and mantle upwelling may drive the thickening and formation of short-lived asymmetric downwellings (e.g., 10, 44). The analysis presented here allows for the identification of a number of these events, including our newly identified short-lived downwelling event along the southern margin of the EPT (see Section 4.3) and successive post-3.1 Ga events outboard of the WPS (corresponding to the Orpheus, Maitland River and Sisters supersuites). These events may have produced the prerequisite metasomatism of the lithospheric mantle tapped by transtension in pull-apart basins to produce sanukitoids within the CPTZ, which correspond to blips of high Ba/Th, La/Sm, $Sm/Yb_{PM,}$ and Sr/Y contours in the Mesoarchean time slices (56, 92).

The low values of Sr/Y, Sm/Yb_{PM}, La/Sm and high Zr/Ti within the vast majority of EPT and Paleoarchean portions of the Karratha Terrane are also consistent with relatively shallow crustal reworking as the predominant mechanism of magma genesis within these lithotectonic blocks from 3.2 Ga onwards. The near-complete absence of high-pressure signatures from these blocks suggests that lithospheric thinning and associated instability ceased to operate by the beginning of the Mesoarchean as the craton progressively stabilized. The episodes of rifting in the Pilbara, likely as short as a few ~10s of Myr, the progressive stretching of the lithosphere, the triggering of lateral asymmetric drips, where fluid-fluxed melting of the mantle occurs, and the following cessation of major tectonics are compatible with the progressive formation and stabilization of craton proposed by numerical modelling (11). In this context, short-lived rifting episodes and associated lateral downwelling form in the initial stage until a stiff, depleted peridotite keel has thickened enough to stabilize the craton. This process is estimated to occur in <500 Myr (10, 11), which is compatible with the ~700 Myr lifecycle of the Pilbara. Thus, the post-cratonization

(<2.9 Ga) shallow re-melting of granitic crust in the EPT that produced potassic magmas (low Sr/Y, Sm/Yb_{PM}, La/Sm; high Zr/Ti) may have been triggered by other mechanisms, such as lithospheric delamination or upwellings (64, 93).

4.3. A 3.06 Ga dripduction event in the East Pilbara Terrane?

The time-space distinction of data further allows the identification of localized events that otherwise would be overlooked in craton-wide datasets but are too large to be identified in a single intrusion. Our results provide the first robust evidence compatible with a dripduction event that affected the exposed southern margin of the EPT coinciding with the emplacement of the Elizabeth Hill Supersuite at 3.06 Ga. This event was previously speculated by Hickman (93) on the basis of east-southeasterly striking linear structures within the southern portion of Yule Dome, which are distinct from the dominant north-northeast structural trend in the rest of the EPT. However, in the absence of geochemical data, the origin of these structural trends remained highly speculative and could also have been attributed to the Proterozoic Ophthalmia and Capricorn orogenies. The zone of high Sr/Y, Sm/Yb_{PM}, La/Sm and Ba/Th within the southern portion of Yule Dome (Fig 4A, B, C, Fig. S7B) indicates that magmatism in this area was the product of high-pressure, fluid-present, low-degree melting in the garnet stability field. An asymmetric downwelling event in a short-lived dripduction zone provides a reasonable explanation for the occurrence of these signatures observed in the Elizabeth Hill Supersuite. The protracted mantle-derived magmatism since 3.45 Ga in the immediate vicinity and lack of other fluid-mediated, deep melting signatures within the EPT after 3.2 Ga is compatible with the development of a buoyant lithospheric keel, which would inhibit vertical drips. However, it could induce inward-dipping asymmetric downwellings in the surrounding, less differentiated lithosphere during lateral movement of the lithotectonic block.

5. Conclusions and implications: from local to global tectonics in the Archean

The geochemical features outlined above represent a relatively complete tectonomagmatic sequence that reflects the development of a local mobile lid-like regime during the maturation of the Pilbara Craton (Fig. 5) and provides novel clues on the tectonics of the Archean. We demonstrate the role of cratonic architecture in imparting geochemical signatures upon granitoids that can be used to reconstruct the tectonic history of a craton. In addition, we posit that the breakup of proto-cratons through rifting is a viable mechanism of craton formation and expansion, as evidenced by the formation of the CPTZ.

These results support the notion that early cratons were not as rigidly immobile as previously envisaged (e.g., 94, 95) and, on the contrary, show quite active tectonics during their formation and stabilization (e.g., 3, 11, 96, 97). Previous numerical modelling studies have demonstrated that craton formation requires a mobile lid-like regime to thin the lithosphere and produce the degrees of mantle depletion necessary for lithospheric keel formation (10-12). Our results provide key natural evidence for the operation of a tectonic style by the Mesoarchean that was dominated by some degree of mobility. These include small amounts of rifting, which are best represented by the ca. 3.2 Ga East Pilbara Terrane Rifting Event (Fig. 5B) and possibly earlier events within the Paleoarchean Ancestral Pilbara Block, as well as minor convergence. These are illustrated by the successive post-3.15 Ga dripduction events interpreted to have produced (among others) the Whundo Group and Railway Supersuite of the Sholl Terrane and the Elizabeth Hill Supersuite along the exposed southern margin of the EPT (Figs. 4, 5C). The observed geochemical signatures and the processes from which they arise need not require an active lid regime and may be the expression of a sluggish lid regime (3), but this cannot be clearly observed. A sluggish lid regime has minor mobility, localized between older, rigid

blocks. This differs from plate tectonics, as this tectonic regime implies the existence of proto-plates without clearly defined plate margins. The Paleoarchean Ancestral Pilbara Block may have operated under a similar mode, but it is also entirely possible that it operated under a squishy lid regime (96, 97) or as the stagnant portion of a larger lid-and-plate regime (10). Such speculations merit future investigation and are beyond the scope of this paper.

The Mesoarchean tectonic regime inferred for the Pilbara is similar to what is believed to be ongoing on Venus, in which locally mobile crustal blocks (campi) move relative to one another in response to mantle convection; this is referred to as the "jostling ice pack" model (98). These campi can fragment over time and are bound by deformational ridge and groove belts that show evidence of lateral motions. In this way, the evolution of the Pilbara may be similar to the fragmentation of a campus; initial fragmentation of the Ancestral Pilbara Block under extensional stress is manifested by the East Pilbara Terrane Rifting Event, where the CPTZ is analogous to a bounding ridge and groove belt. Subsequent lateral motions of the EPT and Karratha Terrane are accommodated within the CPTZ as transtensional, extensional and compressional features. Our geochemical data suggest that magmatic geochemical estimates of the transition to plate tectonics should be treated with caution and cannot be the only line of evidence taken into consideration. Due to the viability of local mobile lid-like features in a sluggish lid world, time-sliced geochemical contour mapping may provide valuable inferences on the local tectonic style of each craton, which, when combined, can ultimately inform our understanding of the greater global geodynamic regime of the early Earth. Given the hypothesized occurrence of TTGs on Venus (99) without clear evidence for a mobile lid regime (100-102), these insights into Earth's early history may have vital extra-terrestrial implications.

Acknowledgments

We are grateful to editor Arturo Gomez-Tuena, and reviewers Tim Johnson and Carlos Ganade for their insightful and thorough comments that have significantly improved our manuscript. We thank Jack Lowrey for coordinating laboratory analyses of collected samples and David Champion for providing contextual information on repository samples. RHS publishes with the permission of the Executive Director of the Geological Survey of Western Australia.

Funding

This project was funded by the Australian Research Council (FL160100168, DP180100580).

Author contributions

EDV, ON, RHS and PAC designed the study. EDV and ON designed the methodology. EDV, ON, RHS, FAC, LM, PAC, MAM, EB and JFM collected the samples. ON, PAC, YNJ and XW provided supervision to this study. EDV compiled the data for the database and created the contour maps. EDV created the figures and performed data interpretations with input from all authors. FAC provided insights into the geodynamic significance of the results. EDV wrote the first draft of the manuscript, which was edited by ON, RHS, FAC, LM, PAC, MAM, EB and JFM.

Competing interests

The authors declare that they have no known competing financial interests or personal relationships that could have appeared to influence the work reported in this paper.

Data and materials availability

All data needed to evaluate the conclusions in the paper are present in the paper and/or the Supplementary Materials. Furthermore, the raw datasets related to this article can be found at https://www.dmp.wa.gov.au/geochem (49), https://dmpbookshop.eruditetechnologies.com.au/product/compilation-of-geochronology-

information-2020.do (50), https://dasc.dmirs.wa.gov.au (51), and

http://pid.geoscience.gov.au/dataset/ga/129306 (52).

Supplementary Materials

Please see the attached word and excel spreadsheet (.xlsx) files.

References

1. B. S. Kamber, E. L. Tomlinson, Petrological, mineralogical and geochemical peculiarities of Archaean cratons. *Chem. Geol.* **511**, 123–151 (2019).

2. R. Stern, W. Bleeker, Age of the world's oldest rocks refined using Canada's SHRIMP: The Acasta Gneiss Complex, Northwest Territories, Canada. *Geoscience Canada* **25**, 27–31 (1998).

3. A. Lenardic, The diversity of tectonic modes and thoughts about transitions between them. *Philos. Trans. R. Soc. A Math. Phys. Eng. Sci.* **376** (2018), doi:10.1098/rsta.2017.0416.

4. T. E. Johnson, M. Brown, B. J. P. Kaus, J. A. Vantongeren, Delamination and recycling of Archaean crust caused by gravitational instabilities. *Nat. Geosci.* **7**, 47–52 (2014).

5. T. E. Johnson, M. Brown, N. J. Gardiner, C. L. Kirkland, R. H. Smithies, Earth's first stable continents did not form by subduction. *Nature*. **543**, 239–242 (2017).

6. J. F. Moyen, H. Martin, Forty years of TTG research. *Lithos*. **148**, 312–336 (2012).

7. T. E. Johnson, C. L. Kirkland, N. J. Gardiner, M. Brown, R. H. Smithies, M. Santosh, Secular change in TTG compositions: Implications for the evolution of Archaean geodynamics. *Earth Planet. Sci. Lett.* **505**, 65–75 (2019).

8. C. B. Keller, B. Schoene, Statistical geochemistry reveals disruption in secular lithospheric evolution about 2.5 Gyr ago. *Nature*. **485**, 490–493 (2012).

9. J. F. Moyen, O. Laurent, Archaean tectonic systems: A view from igneous rocks. Lithos. 302–303, 99–125 (2018).

10. F. A. Capitanio, O. Nebel, P. A. Cawood, R. F. Weinberg, F. Clos, Lithosphere differentiation in the early Earth controls Archean tectonics. *Earth Planet. Sci. Lett.* **525**, 115755 (2019).

11. F. A. Capitanio, O. Nebel, P. A. Cawood, Thermochemical lithosphere differentiation and the origin of cratonic mantle. *Nature*. **588**, 89–94 (2020).

12. F. A. Capitanio, O. Nebel, J. Moyen, P. A. Cawood, Craton formation in early Earth mantle convection regimes. *J. Geophys. Res. Solid Earth* (2022) doi:10.1029/2021jb023911.

13. O. Laurent, H. Martin, J. F. Moyen, R. Doucelance, The diversity and evolution of late-Archean granitoids: Evidence for the onset of "modern-style" plate tectonics between 3.0 and 2.5 Ga. *Lithos.* **205**, 208–235 (2014).

14. S. Ferrero, I. Wannhoff, O. Laurent, C. Yakymchuk, R. Darling, B. Wunder, A. Borghini, P. J. O. Brien, Embryos of TTGs in Gore Mountain garnet megacrysts from water-fluxed melting of the lower crust. *Earth Planet. Sci. Lett.* **569**, 117058 (2021).

15. M. I. H. Hartnady, T. E. Johnson, S. Schorn, R. H. Smithies, C. L. Kirkland, S. H. Richardson, Fluid processes in the early Earth and the growth of continents. *Earth Planet. Sci. Lett.* **594**, 117695 (2022).

16. C. G. Barnes, K. Werts, V. Memeti, K. Ardill, Most granitoid rocks are cumulates: Deductions from hornblende compositions and zircon saturation. *J. Petrol.* **60**, 2240–2277 (2020).

17. J. Kendrick, M. Duguet, C. Yakymchuk, Diversification of Archean tonalite-trondhjemite-granodiorite suites in a mushy middle crust. *Geology*. **50**, 76–80 (2022).

18. O. Laurent, J. Björnsen, J. F. Wotzlaw, S. Bretscher, M. Pimenta Silva, J. F. Moyen, P. Ulmer, O. Bachmann, Earth's earliest granitoids are crystal-rich magma reservoirs tapped by silicic eruptions. *Nat. Geosci.* **13**, 163–169 (2020).

19. H. Rollinson, Do all Archaean TTG rock compositions represent former melts? *Precambrian Res.* **367**, 106448 (2021).

20. R. Fischer, T. Gerya, Early Earth plume-lid tectonics: A high-resolution 3D numerical modelling approach. *J. Geodyn.* **100**, 198–214 (2016).

21. R. Fischer, T. Gerya, Regimes of subduction and lithospheric dynamics in the Precambrian: 3D thermomechanical modelling. *Gondwana Res.* **37**, 53–70 (2016).

22. P. Chowdhury, T. Gerya, S. Chakraborty, Emergence of silicic continents as the lower crust peels off on a hot plate-tectonic Earth. *Nat. Geosci.* **10**, 698–703 (2017).

23. T. E. Johnson, N. J. Gardiner, K. Miljković, C. J. Spencer, C. L. Kirkland, P. A. Bland, H. Smithies, An impact melt origin for Earth's oldest known evolved rocks. *Nat. Geosci.* **11**, 795–799 (2018).

24. T. E. Johnson, C. L. Kirkland, Y. Lu, R. H. Smithies, M. Brown, M. I. H. Hartnady, Giant impacts and the origin and evolution of continents. *Nature*. **608** (2022), doi:10.1038/s41586-022-04956-y.

25. P. Chowdhury, S. Chakraborty, T. V. Gerya, P. A. Cawood, F. A. Capitanio, Peel-back controlled lithospheric convergence explains the secular transitions in Archean metamorphism and magmatism. *Earth Planet. Sci. Lett.* **538**, 116224 (2020).

26. A. Piccolo, B. J. P. Kaus, R. W. White, R. M. Palin, G. S. Reuber, Plume — Lid interactions during the Archean and implications for the generation of early continental terranes. *Gondwana Res.* **88**, 150–168 (2020).

27. E. Sizova, T. Gerya, K. Stüwe, M. Brown, Generation of felsic crust in the Archean: A geodynamic modeling perspective. *Precambrian Res.* **271**, 198–224 (2015).

28. J. Van Hunen, J. F. Moyen, Archean subduction: Fact or fiction? *Annu. Rev. Earth Planet. Sci.* **40**, 195–219 (2012).

29. J. van Hunen, A. P. van den Berg, Plate tectonics on the early Earth: Limitations imposed by strength and buoyancy of subducted lithosphere. *Lithos.* **103**, 217–235 (2008).

30. V. Debaille, C. O'Neill, A. D. Brandon, P. Haenecour, Q. Z. Yin, N. Mattielli, A. H. Treiman, Stagnant-lid tectonics in early Earth revealed by 142Nd variations in late Archean rocks. *Earth Planet. Sci. Lett.* **373**, 83–92 (2013).

31. J. Korenaga, Crustal evolution and mantle dynamics through Earth history. *Philos. Trans. R. Soc. A Math. Phys. Eng. Sci.* **376** (2018), doi:10.1098/rsta.2017.0408.

32. Y. Nebel-Jacobsen, C. Nebel, M. Wille, P. A. Cawood, A non-zircon Hf isotope record in Archean black shales from the Pilbara craton confirms changing crustal dynamics ca. 3 Ga ago. *Sci. Rep.* **8**, 1–7 (2018).

33. M. Tang, K. Chen, R. L. Rudnick, Archean upper crust transition from mafic to felsic marks the onset of plate tectonics. *Science (80-.).* **351**, 372–375 (2016).

34. B. Dhuime, C. J. Hawkesworth, P. A. Cawood, C. D. Storey, A change in the geodynamics of continental growth 3 billion years ago. *Science (80-.).* **335**, 1334–1336 (2012).

35. B. Keller, B. Schoene, Plate tectonics and continental basaltic geochemistry throughout Earth history. *Earth Planet. Sci. Lett.* **481**, 290–304 (2018).

36. N. D. Greber, N. Dauphas, The chemistry of fine-grained terrigenous sediments reveals a chemically evolved Paleoarchean emerged crust. *Geochim. Cosmochim. Acta*. **255**, 247–264 (2019).

37. S. A. Caton, M. A. Smit, R. B. Emo, K. A. Musiyachenko, M. Kielman-Schmitt, E. Kooijman, A. Scherstén, J. Halla, W. Bleeker, J. E. Hoffmann, O. P. Pandey, A. Ravindran, A. Maltese, K. Mezger, Evolution of the sources of TTG and associated rocks during the Archean from in-situ 87Sr/86Sr isotope analysis of apatite by LA-MC-ICPMS. *Lithos*. **428**–**429**, 106830 (2022).

38. M. J. Van Kranendonk, R. Hugh Smithies, A. H. Hickman, D. C. Champion, Review: Secular tectonic evolution of Archean continental crust: interplay between horizontal and vertical processes in the formation of the Pilbara Craton, Australia. *Terra Nov.* **19**, 1–38 (2007).

39. M. J. Van Kranendonk, R. Hugh Smithies, A. H. Hickman, M. T. D. Wingate, S. Bodorkos, Evidence for Mesoarchean (~3.2 Ga) rifting of the Pilbara Craton: The missing link in an early Precambrian Wilson cycle. *Precambrian Res.* **177**, 145–161 (2010).

40. W. J. Collins, M. J. Van Kranendonk, Model for the development of kyanite during partial convective overturn of Archean granite–greenstone terranes: the Pilbara Craton, Australia. *J. Metamorph. Geol.* **17**, 145–156 (1999).

41. M. J. Van Kranendonk, A. H. Hickman, R. H. Smithies, D. R. Nelson, Geology and tectonic evolution of the Archean North Pilbara Terrain, Pilbara Craton, Western Australia. *Econ. Geol.* **97**, 695–732 (2002).

42. A. H. Hickman, Review of the Pilbara Craton and Fortescue Basin, Western Australia: Crustal evolution providing environments for early life. *Isl. Arc*. **21**, 1–31 (2012).

43. P. A. Cawood, C. J. Hawkesworth, S. A. Pisarevsky, B. Dhuime, F. A. Capitanio, O. Nebel, Geological archive of the onset of plate tectonics. *Philos. Trans. R. Soc. A Math. Phys. Eng. Sci.* **376** (2018), doi:10.1098/rsta.2017.0405.

44. O. Nebel, F. A. Capitanio, J. F. Moyen, R. F. Weinberg, F. Clos, Y. J. Nebel-Jacobsen, P. A. Cawood, When crust comes of age: On the chemical evolution of Archaean, felsic continental crust by crustal drip tectonics. *Philos. Trans. R. Soc. A Math. Phys. Eng. Sci.* **376** (2018), doi:10.1098/rsta.2018.0103.

45. W. S. Bowman, Canadian Diorite Gneiss SY-4: Preparation and Certification by Eighty-Nine International Laboratories. *Geostand. Geoanalytical Res.* **19**, 101–124 (1995).

46. [dataset] C.L. Hamlyn, Datapack for OREAS 24b. (OREAS Reference Materials, 2012; https://www.oreas.com/downloads/?fileId=1594).

47. K. P. Jochum, U. Weis, B. Schwager, B. Stoll, S. A. Wilson, G. H. Haug, M. O. Andreae, J. Enzweiler, Reference Values Following ISO Guidelines for Frequently Requested Rock Reference Materials. *Geostand. Geoanalytical Res.* **40**, 333–350 (2016).

48. Q. Liang, D. C. Grégoire, Determination of trace elements in twenty six Chinese geochemistry reference materials by inductively coupled plasma-mass spectrometry. *Geostand. Newsl.* **24**, 51–63 (2000).

49. [dataset] Geological Survey of Western Australia, GeoChem Extract: Western Australian Geochemistry (WACHEM) database. (Department of Mines, Industry Regulation and Safety, 2022; https://www.dmp.wa.gov.au/geochem).

50. [dataset] Geological Survey of Western Australia, Geological Survey of Western Australia Compilation of Geochronology Information, 2020. (Department of Mines, Industry Regulation and Safety, 2020; https://dmpbookshop.eruditetechnologies.com.au/product/compilation-of-geochronology-information-2020.do).

51. [dataset] Geological Survey of Western Australia, 1:500 000 State interpreted bedrock geology of Western Australia, June 2020 update. (Department of Mines, Industry Regulation and Safety, 2020; https://dasc.dmirs.wa.gov.au).

52. [dataset] Geoscience Australia, Inorganic Geochemistry Database. (Geoscience Australia, Canberra, 2019; http://pid.geoscience.gov.au/dataset/ga/129306).

53. D.C. Champion, R.H. Smithies, Geochemistry of Paleoarchean granites of the East Pilbara terrane, Pilbara craton, Western Australia: implications for Early Archean crustal growth. *Developments in Precambrian Geology* **15**, 369-409 (2007).

54. J. F. Moyen, The composite Archaean grey gneisses: Petrological significance, and evidence for a non-unique tectonic setting for Archaean crustal growth. *Lithos*. **123**, 21–36 (2011).

55. J. F. Moyen, Archean granitoids: classification, petrology, geochemistry and origin. *Geol. Soc. Spec. Publ.* **489**, 15–49 (2020).

56. R. H. Smithies, Y. Lu, C. L. Kirkland, T. E. Johnson, D. R. Mole, D. C. Champion, L. Martin, H. Jeon, M. T. D. Wingate, S. P. Johnson, Oxygen isotopes trace the origins of Earth's earliest continental crust. *Nature*. **592**, 70–75 (2021).

57. H. Martin, J. F. Moyen, M. Guitreau, J. Blichert-Toft, J. L. Le Pennec, Why Archaean TTG cannot be generated by MORB melting in subduction zones. *Lithos*. **198**–**199**, 1–13 (2014).

58. H. Martin, J. F. Moyen, R. Rapp, The sanukitoid series: Magmatism at the Archaean-Proterozoic transition. *Earth Environ. Sci. Trans. R. Soc. Edinburgh*. **100**, 15–33 (2009).

59. R. H. Smithies, D. C. Champion, The Archaean high-Mg diorite suite: Links to Tonalite-Trondhjemite-Granodiorite magmatism and implications for early Archaean crustal growth. *J. Petrol.* **41**, 1653–1671 (2000).

60. D. R. Mole, P. C. Thurston, J. H. Marsh, R. A. Stern, J. A. Ayer, L. A. J. Martin, Y. J. Lu, The formation of Neoarchean continental crust in the south-east Superior Craton by two distinct geodynamic processes. *Precambrian Res.* **356** (2021), doi:10.1016/j.precamres.2021.106104.

61. R.H. Smithies, Y. Lu, K. Gessner, M. Wingate, D. Champion, Geochemistry of Archean granitic rocks in the South West Terrane of the Yilgarn Craton (GSWA Record 2018/10, 2018).

62. D. C. Champion, R. H. Smithies, "Geochemistry of Paleoarchean Granites of the East Pilbara Terrane, Pilbara Craton, Western Australia" in *Earth's Oldest Rocks*, M. J. Van Kranendonk, V. C. Bennett, J. E. Hoffmann, Eds. (Elsevier B.V., ed. 2, 2019; http://dx.doi.org/10.1016/B978-0-444-63901-1.00021-6), pp. 487–518.

63. J. F. Moyen, D. Champion, R. H. Smithies, The geochemistry of Archaean plagioclase-rich granites as a marker of source enrichment and depth of melting. *Earth Environ. Sci. Trans. R. Soc. Edinburgh*. **100**, 35–50 (2009).

64. N. J. Gardiner, A. H. Hickman, C. L. Kirkland, Y. Lu, T. Johnson, J. X. Zhao, Processes of crust formation in the early Earth imaged through Hf isotopes from the East Pilbara Terrane. *Precambrian Res.* **297**, 56–76 (2017).

65. D. R. Mole, C. L. Kirkland, M. L. Fiorentini, S. J. Barnes, K. F. Cassidy, C. Isaac, E. A. Belousova, M. Hartnady, N. Thebaud, Time-space evolution of an Archean craton: A Hf-isotope window into continent formation. *Earth-Science Rev.* **196**, 102831 (2019).

66. W. F. McDonough, S. -s. Sun, The composition of the Earth. *Chem. Geol.* **120**, 223–253 (1995).

67. J. F. Moyen, G. Stevens, Experimental constraints on TTG petrogenesis: Implications for Archean geodynamics. *Geophys. Monogr. Ser.* **164**, 149–175 (2006).

68. J. A. Winchester, P. A. Floyd, Geochemical discrimination of different magma series and their differentiation products using immobile elements. *Chem. Geol.* **20**, 325–343 (1977).

69. J. Pearce, A User's Guide to Basalt Discrimination Diagrams. *Geol. Assoc. Canada Short Course Notes*. **12**, 79–113 (1996).

70. T. Elliott, Tracers of the slab. *Geophys. Monogr. Ser.* **138**, 23–45 (2004).

71. J. D. Hernández-Montenegro, R. M. Palin, C. A. Zuluaga, D. Hernández-Uribe, Archean continental crust formed by magma hybridization and voluminous partial melting. *Sci. Rep.* **11**, 1–9 (2021).

72. A. H. Hickman, M. J. Van Kranendonk, Early Earth evolution : evidence from the 3.5–1.8 Ga geological history of the Pilbara region of Western Australia. *Episodes*. **35**, 283–297 (2012).

73. J. E. Hoffmann, C. Zhang, J.-F. Moyen, T. J. Nagel, "The Formation of Tonalites–Trondjhemite–Granodiorites in Early Continental Crust" in *Earth's Oldest Rocks*, M. J. Van Kranendonk, V. C. Bennett, J. E. Hoffmann, Eds. (Elsevier B.V., ed. 2, 2019), pp. 133–168.

74. J. Kendrick, C. Yakymchuk, Garnet fractionation, progressive melt loss and bulk composition variations in anatectic metabasites: Complications for interpreting the geodynamic significance of TTGs. *Geosci. Front.* **11**, 745–763 (2020).

75. R. H. Smithies, D. C. Champion, M. J. Van Kranendonk, Formation of Paleoarchean continental crust through infracrustal melting of enriched basalt. *Earth Planet. Sci. Lett.* **281**, 298–306 (2009).

76. R. Tamblyn, J. Hermann, D. Hasterok, P. Sossi, T. Pettke, S. Chatterjee, Hydrated komatiites as a source of water for TTG formation in the Archean. *Earth Planet. Sci. Lett.* **603**, 117982 (2023).

77. A. Pourteau, L. S. Doucet, E. R. Blereau, S. Volante, T. E. Johnson, W. J. Collins, Z. X. Li, D. C. Champion, TTG generation by fluid-fluxed crustal melting: Direct evidence from the Proterozoic Georgetown Inlier, NE Australia. *Earth Planet. Sci. Lett.* **550**, 116548 (2020).

78. R. P. Rapp, E. B. Watson, Dehydration Melting of Metabasalt at 8–32 kbar: Implications for Continental Growth and Crust-Mantle Recycling. *J. Petrol.* **36**, 891–931 (1995).

79. 1. X.-L. Xiong, Trace element evidence for growth of early continental crust by melting of rutile-bearing hydrous eclogite. *Geology*. **34**, 945–948 (2006).

80. H. S. C. O'Neill, The Smoothness and Shapes of Chondrite-normalized Rare Earth Element Patterns in Basalts. *J. Petrol.* **57**, 1463–1508 (2016).

81. R. M. Palin, R. W. White, E. C. R. Green, Partial melting of metabasic rocks and the generation of tonalitic–trondhjemitic–granodioritic (TTG) crust in the Archaean: Constraints from phase equilibrium modelling. *Precambrian Res.* **287**, 73–90 (2016).

82. C. L. Kirkland, P. J. Sutton, T. Erickson, T. E. Johnson, M. J. H. Hartnady, H. Smithies, M. Prause, Did transit through the galactic spiral arms seed crust production on the early Earth? *Geology*. **50**, 1312–1317 (2022).

83. T. Ubide, P. C. Guyett, G. G. Kenny, F. M. O'Sullivan, D. E. Ames, J. A. Petrus, N. Riggs, B. S. Kamber, Protracted volcanism after large impacts: Evidence from the Sudbury impact basin. *J. Geophys. Res. Planets*. **122**, 701–728 (2017).

84. K.C. Condie, Archean greenstone belts. (Elsevier,1981), vol. 3.

85. M. J. Van Kranendonk, R. Hugh Smithies, W. L. Griffin, D. L. Huston, A. H. Hickman, D. C. Champion, C. E. Anhaeusser, F. Pirajno, Making it thick: A volcanic plateau origin of Palaeoarchean continental lithosphere of the Pilbara and Kaapvaal cratons. *Geol. Soc. Spec. Publ.* **389**, 83–111 (2015).

86. J. H. Bédard, A catalytic delamination-driven model for coupled genesis of Archaean crust and sub-continental lithospheric mantle. *Geochim. Cosmochim. Acta*. **70**, 1188–1214 (2006).

87. D. Wiemer, C. E. Schrank, D. T. Murphy, L. Wenham, C. M. Allen, Earth's oldest stable crust in the Pilbara Craton formed by cyclic gravitational overturns. *Nat. Geosci.* **11**, 357–361 (2018).

88. F. A. Capitanio, O. Nebel, P. A. Cawood, R. F. Weinberg, P. Chowdhury, Reconciling thermal regimes and tectonics of the early Earth. *Geology*. **47**, 923–927 (2019).

89. C. Chelle-Michou, A. McCarthy, J. F. Moyen, P. A. Cawood, F. A. Capitanio, Make subductions diverse again. *Earth-Science Rev.* **226**, 1–17 (2022).

90. J. F. Moyen, J. van Hunen, Short-term episodicity of Archean plate tectonics. *Geology*. **40**, 451–454 (2012).

91. R. H. Smithies, D. C. Champion, M. J. Van Kranendonk, H. M. Howard, A. H. Hickman, Modern-style subduction processes in the Mesoarchaean: Geochemical evidence from the 3.12 Ga Whundo intra-oceanic arc. *Earth Planet. Sci. Lett.* **231**, 221–237 (2005).

92. M. A. de Oliveira, R. Dall'agnol, B. Scaillet, Petrological constraints on crystallization conditions of Mesoarchean sanukitoid rocks, southeastern Amazonian craton, Brazil. *J. Petrol.* **51**, 2121–2148 (2010).

93. A. H. Hickman, "East Pilbara Craton: a record of one billion years in the growth of Archean continental crust" (Geological Survey of Western Australia, 2021).

94. J. H. Bédard, Stagnant lids and mantle overturns: Implications for Archaean tectonics, magmagenesis, crustal growth, mantle evolution, and the start of plate tectonics. *Geosci. Front.* **9**, 19–49 (2018).

95. R. J. Stern, The evolution of plate tectonics. *Philos. Trans. R. Soc. A Math. Phys. Eng. Sci.* **376** (2018), doi:10.1098/rsta.2017.0406.

96. D. L. Lourenço, A. B. Rozel, M. D. Ballmer, P. J. Tackley, Plutonic-Squishy Lid: A New Global Tectonic Regime Generated by Intrusive Magmatism on Earth-Like Planets. *Geochemistry, Geophys. Geosystems*. **21** (2020), doi:10.1029/2019GC008756.

97. A. B. Rozel, G. J. Golabek, C. Jain, P. J. Tackley, T. Gerya, Continental crust formation on early Earth controlled by intrusive magmatism. *Nature*. **545**, 332–335 (2017).

98. P. K. Byrne, R. C. Ghail, A. M. C. Şengör, P. B. James, C. Klimczak, S. C. Solomon, A globally fragmented and mobile lithosphere on Venus. *Proc. Natl. Acad. Sci. U. S. A.* **118** (2021), doi:10.1073/pnas.2025919118.

99. Y. J. Wang, J. G. Shellnutt, J. Kung, Y. Iizuka, Y. M. Lai, The formation of tonalitic and granodioritic melt from Venusian basalt. *Sci. Rep.*, 1–8 (2022)

100. L. B. Harris, J. H. Bédard, "Crustal evolution and deformation in a non-plate-tectonic Archaean Earth: Comparisons with Venus" in Evolution of Archean Crust and Early Life, Y. Dilek, H. Furnes, Eds. (Springer, 2014), pp. 215–291.

101. R. J. Phillips, W. M. Kaula, G. E. McGill, M. C. Malin, Tectonics and evolution of Venus. *Science* **212**, 879–887 (1981).

102. D. L. Turcotte, An episodic hypothesis for Venusian tectonics. *J. Geophys. Res.* **98**, 17061–17069 (1993).

103. J.T. O'Connor, A classification of quartz rich igneous rock based on feldspar ratios. (United States Geological Survey, 525B, B79-B84, 1965).

104. J. Pearce, Geochemical Fingerprinting of oceanic basalts with applications to ophiolite classification and the search for Archean oceanic crust. *Lithos* **100**, 14–48 (2008).

105. S-S Sun, W.F. McDonough, “Chemical and isotopic systematics of oceanic basalts: implications for mantle compositions and processes” in *Magmatism in Ocean Basins*, A.D. Saunders, M.J. Norry, Eds, (Geol. Soc. Lond. Spec. Publ., vol. 42, 1989), pp. 313-345.

106. O. Laurent, A. Zeh, G. Brandl, A. Vezinet, A. Wilson, "Granitoids and Greenstone Belts of the Pietersburg Block---Witnesses of an Archaean Accretionary Orogen Along the Northern Edge of the Kaapvaal Craton" in *The Archaean Geology of the Kaapvaal Craton, Southern Africa*, A. Kröner, A. Hofmann, Eds. (Springer International Publishing, Cham, 2019; https://doi.org/10.1007/978-3-319-78652-0_4), pp. 83–107.

Declaration of interests

☒The authors declare that they have no known competing financial interests or personal relationships that could have appeared to influence the work reported in this paper.

☐The authors declare the following financial interests/personal relationships which may be considered as potential competing interests:

Highlights

- Critical review of the tectonomagmatic evolution of the Pilbara Craton from >3.5-2.8 Ga.
- Granitoid whole-rock geochemistry is controlled by discrete lithotectonic blocks.
- 3.2 Ga transition from sodic magmatism to broader magmatic compositional spectrum.
- Mesoarchean mobile lid-like features in weak crust between rigid plateau fragments.
- Features indicative of sluggish lid regime resemble present-day processes on Venus.